

Three-dimensional imaging of shear bands in bulk metallic glass composites

A.H. HUNTER*, V. ARAULLO-PETERS*, M. GIBBONS†, O.D. RESTREPO†, S.R. NIEZGODA†, W. WINDL†, K.M. FLORES‡, D.C. HOFMANN§ & E.A. MARQUIS*

*Department of Materials Science and Engineering, University of Michigan, Ann Arbor, Michigan, U.S.A.

†Department of Materials Science and Engineering, The Ohio State University, Columbus, Ohio, U.S.A.

‡Department of Mechanical Engineering and Materials Science, Institute of Materials Science and Engineering, Washington University, St. Louis, Missouri, U.S.A.

§Jet Propulsion Laboratory/California Institute of Technology, Pasadena, California, U.S.A.

Key words. Atom probe tomography, density-functional theory, shear band.

Summary

The mechanism of the increase in ductility in bulk metallic glass matrix composites over monolithic bulk metallic glasses is to date little understood, primarily because the interplay between dislocations in the crystalline phase and shear bands in the glass could neither be imaged nor modelled in a validated way. To overcome this roadblock, we show that shear bands can be imaged in three dimensions by atom probe tomography from density variations in the reconstructed atomic density, which density-functional theory suggests being a local-work function effect. Imaging of near-interface shear bands in $\text{Ti}_{48}\text{Zr}_{20}\text{V}_{12}\text{Cu}_5\text{Be}_{15}$ bulk metallic glass matrix composite permits measurement of their composition, thickness, branching and interactions with the dendrite interface. These results confirm that shear bands here nucleate from stress concentrations in the glass due to intense, localized plastic deformation in the dendrites rather than intrinsic structural inhomogeneities.

Introduction

Bulk metallic glass materials combine a very high yield strength with the ability to be intricately formed into net shape components using relatively low temperature forging above the material's glass transition temperature. However, at temperatures below the glass transition, bulk metallic glasses frequently display very limited ductility and catastrophic failure due to the propagation of shear bands, which are zones with strongly localized deformation. To improve ductility, bulk metallic glass matrix composites (BMGMCs) have been proposed, where a crystalline dendritic network can redistribute load through dislocation slip (Hays, 2000). Although on the macroscopic level, there is agreement that the crystalline

phase blocks the long-range propagation of shear bands and thus preempts catastrophic failure in BMGMCs, their formation, propagation and interactions with the reinforcing crystalline phase remain under discussion (Chen, 2012, 2013; Jeon, 2013; Zhang, 2014), making targeted improvement of BMGMC alloys very difficult.

Arguably, the largest uncertainties exist concerning the formation processes of shear bands in BMGMCs. Although shear bands are often found to originate from structural flaws, such as voids or surface features, which act as stress concentrations, their formation in monolithic glasses is typically discussed in terms of local inhomogeneities on the level of the ambiguously defined shear transformation zones (Argon, 1979). For BMGMCs, no fundamentally different nucleation mechanism is assumed, and the interplay between deformation mechanisms in the crystalline dendrites and shear band formation in the glass matrix that can lead to large ductility, such as observed for $\text{Ti}_{48}\text{Zr}_{20}\text{V}_{12}\text{Cu}_5\text{Be}_{15}$ BMGMC, is little understood.

Also, shear bands usually appear as a change in the local free volume, which is defined as the volume in excess of an ideal amorphous structure. At times, the structural changes in shear bands are so severe that crystalline phases (Jiang, 2006) or nanovoids (Li, 2002) have been observed following deformation. Although changes in local free volume in shear bands is little disputed in the current literature, large discrepancies exist about their magnitude. Traditionally, localization of strain in shear bands has been associated with increased free volume, or equivalently lower density. This increase ranges from small changes of 1–2% measured with nanobeam diffraction (Chen, 2009) to changes as large as 11% suggested by transmission electron microscopy imaging (Donovan, 1981). To add even larger spread, recent high angle annular dark field (HAADF) scanning transmission electron microscopy (STEM) work reported a decrease in free volume within shear bands (Shao, 2013) with a range of density changes from –10% to +6.3% (Rösner, 2014). The variations are currently

Correspondence to: Emmanuelle Marquis, Department of Materials Science and Engineering, University of Michigan, Ann Arbor, Michigan 48109, U.S.A. Tel: +734-764-8717; e-mail: emarq@umich.edu

unexplained, with possible reasons ranging from stick-slip-like shearing in shear bands to artefacts related to the 2D projection in Z-contrast imaging.

In order to clarify the nature of shear bands, we apply a three-dimensional imaging method based on atom probe tomography (APT), which in combination with STEM imaging and modelling on both atomic and continuum scales gives new key insights into the deformation mechanisms and interplay between the crystalline and glass phases in BMGMCs.

Experimental methods and results

A $\text{Ti}_{48}\text{Zr}_{20}\text{V}_{12}\text{Cu}_5\text{Be}_{15}$ glass composite was arc melted under vacuum and rapidly chilled in a water-cooled copper mould. The sample was machined into a tension test sample and pulled in tension until failure, resulting in a highly deformed necked region with a high density of shear bands.

Samples for APT and transmission electron microscopy were prepared using a FEI Helios Nanolab 650 DualBeam FIB (FEI, Eindhoven, The Netherlands). Transmission electron microscopy (TEM) samples were analysed using a JEOL (Peabody, MA, USA) 2100F TEM/STEM equipped with a spherical aberration corrector at 200 kV accelerating voltage. Images were recorded in STEM mode with HAADF detectors and were analysed using ImageJ (Schneider, 2012). APT samples were analysed using a Cameca (Madison, WI, USA) LEAP 4000X HR atom probe instrument operated in laser pulsed mode. The samples were field evaporated at 25 K using 10 pJ laser pulse energy and 250 kHz pulse repetition rate, with a nominal detection rate of 0.5%. Reconstruction and visualization were performed using the Cameca software IVAS 3.6. Sample geometry was measured before and after APT, and was used to calculate the evaporation field and image compression factor needed for the data reconstruction algorithm. Typical values were 42 V nm^{-1} for the field strength and image compression factors ranging from 1.4 to 1.7. Local densities are calculated from counting the number of ions within a sphere of fixed radius centred on each individual ion. The choice of the radius requires a trade-off between statistical uncertainty in the local density from too small a radius and loss of spatial resolution from a radius that is too large. A value of 1.0 nm was used for this analysis. The shear bands were then imaged using the reconstructed atomic density.

Our APT method is based on density variations, which were first analysed with HAADF STEM imaging in order to define the density range present. In Figure 1, the shear bands, which were aligned parallel to the electron beam, are clearly discernible in the amorphous matrix, appearing darker than the surrounding matrix. This is consistent with a slight reduction in density (or increase in free volume) in the shear bands compared to the surrounding matrix (Rösner, 2014). Measurements of relative intensity changes across the shear bands suggest an average density change of $-3\% \pm 1\%$ using the full width at half maximum

of the density plot to determine the limits, over a gradient of $\sim 3 \text{ nm}$, although no decrease in free volume was found.

The deformed structures analysed by APT reveal shear band regions with higher reconstructed atomic density, in contrast to the HAADF results, which makes them visible in Figure 2. The shear bands are observed in the glass matrix and also near and intersecting the dendrite interface. The thickness of the individual shear bands ranges from 3.4 to 10 nm, with an average thickness (or full width at half maximum of the density peak) of $6 \pm 1.5 \text{ nm}$. This can be compared to known characteristic shear band thickness of $\sim 10 \text{ nm}$ (Zhang, 2006). No detectable chemistry change was measured through 1D concentration analysis perpendicular to the band (Fig. 2B), which is consistent with previous APT studies (Chen, 2009; Guo, 2014). In addition, no evidence of local chemical clustering was detected. Quantitatively, the shear band regions exhibit an average reconstructed atomic density increase of 20% ranging from 7% to 60% (Fig. 2C).

Modelling

To understand the apparent contradiction between the shear band densities observed by APT and HAADF, we examined the dependence of the evaporation field on the density of the sample using density-functional theory calculations using within the image-hump model (Müller, 1956). Although the underlying model has been criticized (Miller, 2014) and does not produce correct escape distances (Yao, 2015), previous density-functional theory work has suggested that it agrees with field-dependent calculations for Al in the evaporation regime rather well (Sanchez, 2004). Within the image-hump model (Müller, 1956), the evaporation field in the low-temperature limit is given by

$$F_0^{n+} = 4\pi(ne)^{-3}(Q_{n+}^0)^2, \quad (1)$$

where ne is the escape charge and Q_{n+}^0 is a thermodynamic term given by $Q_{n+}^0 = H_b + I_{n+} - n\phi$, which can be calculated from the binding enthalpy of the (neutral) atom H_b , its ionization energy from charge 0 to $n+$, I_{n+} and the local work function ϕ (Smith, 1930). The neutral-atom binding energy was calculated as the enthalpy ($H = E_{\text{tot}} + pV$) difference between the perfect surface with an isolated atom in the centre of the vacuum layer and the perfect surface with an adatom on the hollow site. We used the density-functional theory code VASP (Kresse, 1994) with projector augmented wave (PAW) potentials within PW-91 spin-resolved generalized gradient approximation (GGA) (Perdew, 1992) with 240 eV cut-off energy. Work function and neutral-atom binding energy are calculated with $3 \times 3 \times 3$ supercells of the conventional face-centered cubic (fcc) unit cell with 108 atoms, a 1.5-nm vacuum and relaxed (100) surfaces with $4 \times 4 \times 1$ k -point Brillouin zone sampling. The entire structure was scaled isotropically to examine different densities that were calculated from the in-plane lattice constants. The work

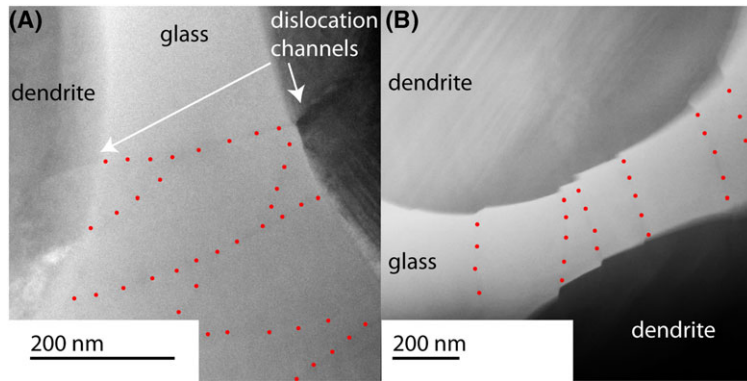


Fig. 1. HAADF STEM images of shear bands in metallic glass matrix and corresponding shear steps on dendrite interfaces. (A) The shear bands are observed to bend, branch and intersect with other shear bands as they propagate from one dendrite arm to an adjacent arm. In (B) the shear bands are decorated with red dots to depict the branching. The shear bands begin and terminate at shear steps on the dendrite interface.

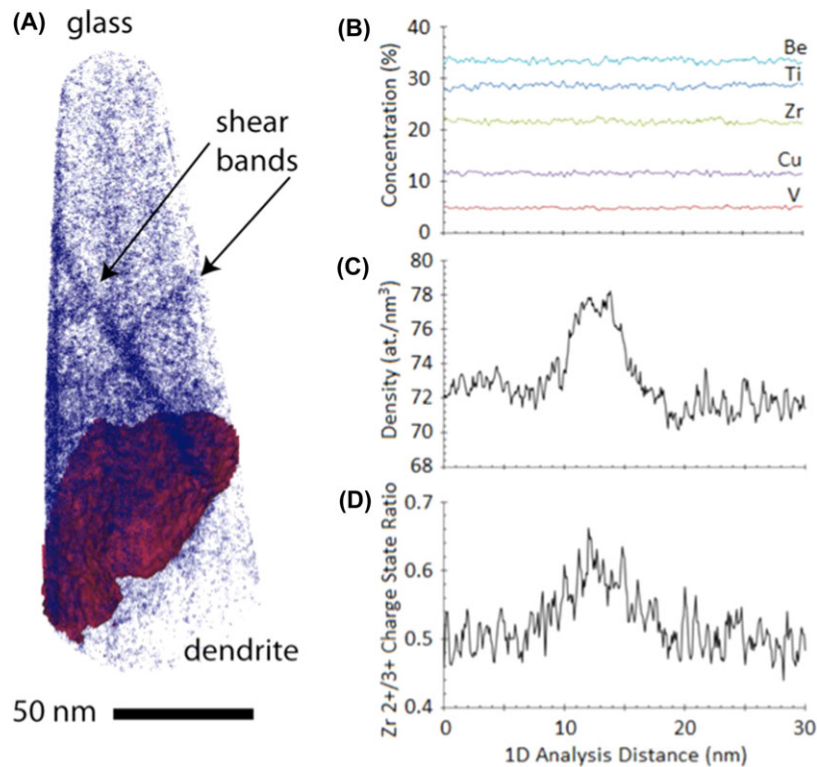


Fig. 2. (A) APT reconstructions containing multiple shear bands. The interface between both phases is marked by a 34% at Ti iso-concentration surface (red). Note that 15% of the atoms with a local density greater than 90 at./nm^3 are shown by blue. (B) 1D profile taken across representative shear band detected by APT. No significant concentration variation is detected between the SB and the matrix (B), but an increase in both reconstructed density (C) and Zr 2+/3+ charge-state ratio (D) are observed within the shear band.

function was calculated from the difference between the calculated electrostatic potential in the centre of the vacuum and the calculated Fermi energy and is 4.23 eV for the relaxed cell, very close to the experimental value of 4.24 eV. The ionization energy is calculated from the energy difference between neutral and charged atoms in vacuum for different simulation cell sizes a between 15 and 3.0 nm side

length and extrapolated to infinity by fitting $E(a) = E_\infty - E'/a$. It is found to be 6.04 eV for Al^+ and 24.87 eV for Al^{++} , in good agreement with experimental values of 5.99 and 24.81 eV (Lide, 2003). For the relaxed structure, we find binding energies $Q_1^0 = 4.9 \text{ eV}$ and $Q_2^0 = 19.4 \text{ eV}$, resulting in zero-temperature evaporation fields $F_0^1 = 17 \text{ V nm}^{-1}$ and $F_0^2 = 33 \text{ V nm}^{-1}$, in good agreement with previously calculated

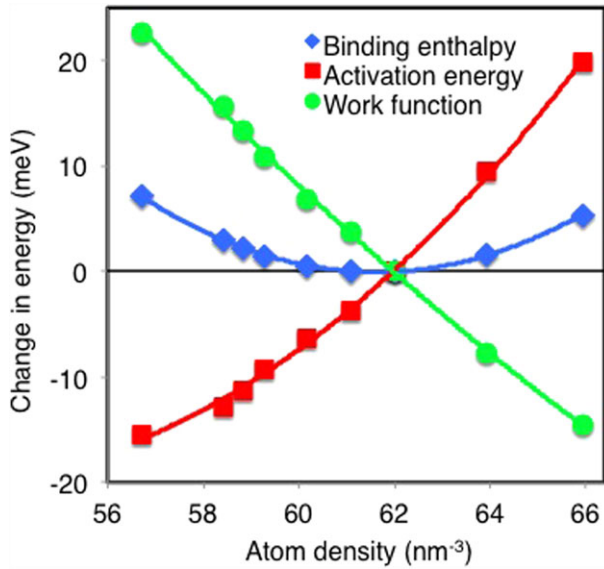


Fig. 3. Dependence of the ion binding energy for Al⁺ and its components on the density in bulk Al as calculated by DFT. This shows that the evaporation field which is proportional to the square of the binding energy will decrease with decreasing density.

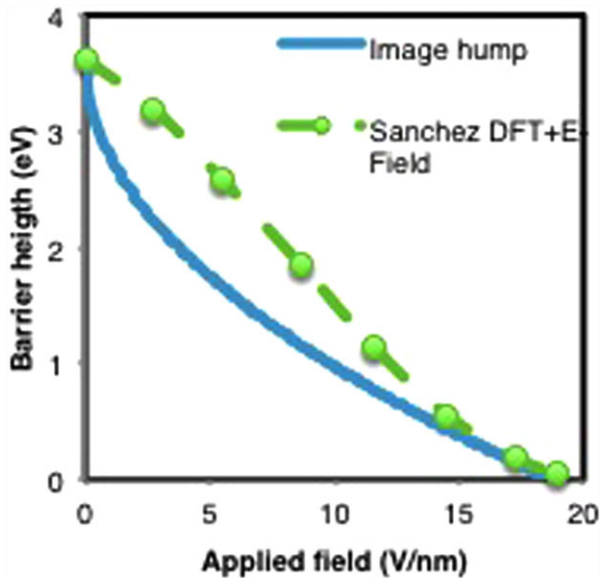


Fig. 4. Barrier height versus applied field values from ref. Sanchez (2004) + image-hump model for which the thermodynamic term is taken from Sanchez' value for zero field.

values of 19 and 35 V nm⁻¹, respectively (Tsong, 1978).

Significantly decreasing computational uncertainties and cost by substituting a bulk metallic glass structure with an isolated adatom on an Al surface, allows us then to derive a scaling law for the change in evaporation field with density. The simulation cell was scaled isotropically and its density

was calculated from the in-plane lattice constants. Figure 3 shows the results for relative changes in heat of evaporation (sum of total energy of evaporation plus pV term for the bulk of the slab), work function and resulting activation energy as a function of atom density relative to the minimum-energy density at 62.03 atoms nm⁻³. Note that the ionization energy of the ion is independent of the bulk density. Although the binding enthalpy is approximately symmetric around the minimum volume with little skew from the pV term, the work function is monotonically increasing with decreasing density. This results in the overall binding energy and thus evaporation field decreasing as a function of decreasing density, in agreement with our experimental finding. Thus, we find that it is the density dependence of the local work function that ultimately causes the artefact of higher observed densities in APT for lower-density material. This modelling prediction can be further validated by looking at the charge–state ratios of the evaporating ions.

In order to determine the dependence of the charge–state ratio on density for an ion species with charges n and m , we start from the density-dependent activation energy for field evaporation for the two charge states in the presence of the field, which is given by (Müller, 1956):

$$Q_{n+}(F, \rho) = H_b(\rho) + I_{n+} - n\phi(\rho) - \sqrt{\frac{n^3 e^3 F}{4\pi \epsilon_0}}. \quad (2)$$

Due to the limitations of image-hump model, we examine here if it is sufficient for our purposes and describes the barrier dependence on field reasonably well in the range where the barrier disappears, i.e. where field evaporation happens. For that, we plot in Figure 4 the results from Sanchez (2004), along with barrier versus field derived from the image-hump model (Eq. (2)) using the barrier value of 3.6 eV for $F = 0$, i.e. $Q_{1+}(F) = Q_{1+}^{\text{Sanchez}}(F = 0) - \sqrt{\frac{n^3 e^3 F}{4\pi \epsilon_0}}$. Evaporation happens where the barrier disappears, i.e. for fields around 19 V nm⁻¹. As can be seen, the value for the evaporation field, as well as the slope of barrier versus field, show rather good agreement between image-hump prediction and directly calculated values. Thus, independently of whether this agreement is physical or fortuitous, it means that Eq. (2) along with Eq. (1) in the main text provide a model to derive the dependence of zero-barrier evaporation fields on density.

Since the evaporation rates r_{n+} can be assumed to follow an Arrhenius behaviour,

$$r_{n+}(F, \rho) = r_0 \exp\left(-\frac{Q_{n+}(F, \rho)}{kT}\right), \quad (3)$$

the change in evaporation rate ratio with density is given by

$$\frac{r_{n+}(F, \rho)}{r_{m+}(F, \rho)} = \exp\left(-\frac{Q_{n+}(F, \rho) - Q_{m+}(F, \rho)}{kT}\right), \quad (4)$$

assuming that the dependence of the prefactor on density can be neglected, which has been shown previously to be a good approximation for bulk-activated processes (Laudon, 2001).

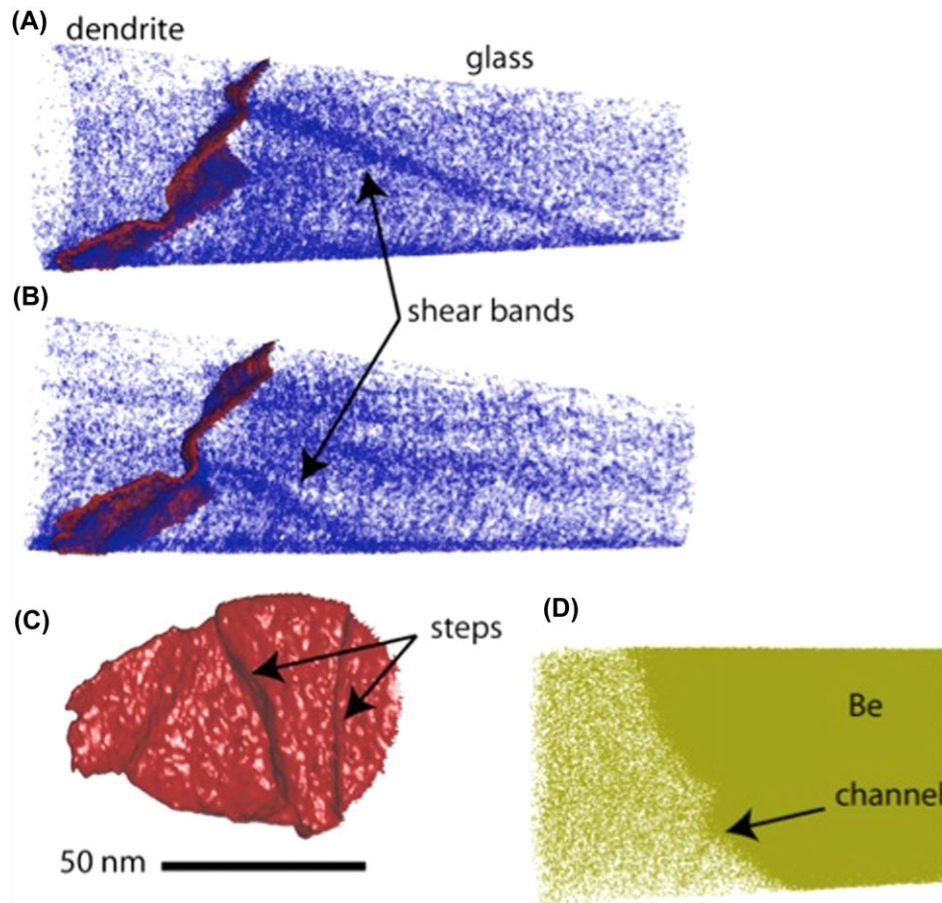


Fig. 5. APT reconstruction showing shear bands terminating at the dendrite interface. (A) and (B) are rotated views of the same tip showing two shear steps at the interface. (C) is a top-down view of the 42% Ti isoconcentration surface showing both interface steps. (D) shows the partitioning map of Be across the dendrite-glass interface, which appears to segregate to the shear band near the step in the dendrite (C).

Since the density dependence of the work function dominates that of the binding enthalpy (Fig. 4), the overall relative change in charge-state ratio for two densities ρ_1 and ρ_2 is then given by the density dependence of the work function,

$$R_{n+/m+}(\rho_1, \rho_2) = \frac{\left[\frac{r_{n+}(F, \rho_1)}{r_{m+}(F, \rho_1)} \right]}{\left[\frac{r_{n+}(F, \rho_2)}{r_{m+}(F, \rho_2)} \right]} = \exp \left[(n - m) \frac{\phi(\rho_1) - \phi(\rho_2)}{kT} \right]. \quad (5)$$

If we assume that the increase in work function of +6.8 meV for 3% density decrease calculated for Al is typical and that the evaporation temperature is in the range of 25–90 K, we would expect an increase in the charge-state ratio of ~ 0.04 – 0.4 . The experimentally measured $\text{Zr}^{2+}/\text{Zr}^3$ ratio is enhanced by $\sim 20\%$ within the shear band compared to the matrix (Fig. 2D), which is of similar order of magnitude. The lowered evaporation field leads to increased evaporation rate locally, which manifests itself as a dip in the specimen surface and thus locally focused ion trajectories with adjacent matrix atoms projected into the same region of the detector as the shear band atoms. However,

if properly exploited, the presence of such an artefact is not detrimental to APT analysis, but rather a powerful imaging tool as demonstrated by the present study.

Material microstructure and properties

Without exception, all visible shear bands either terminate at the matrix/dendrite interface or at other shear bands. No evidence could be found of shear bands originating or terminating within the glass matrix. This suggests that processes occurring at the glass/crystalline interface initiate shear bands in the glass, rather than structural inhomogeneities within the glass itself. Furthermore, the observations suggest that localized slip activity within the crystalline phase and associated interfacial steps are coupled with shear band nucleation, propagation and linking of the slip planes from one dendrite arm to another. A range of step heights linking dislocation channels in the dendrites with shear bands in the glass was observed. Where significant deformation had taken place, the shear bands are all connected with 20–50 nm (~ 50 – 150

Burgers vector lengths) or higher steps at the matrix/dendrite interface (Fig. 1A). In Figure 1(B), the interfacial steps are significantly smaller (<10 nm), which agrees well with the APT reconstructions in Figure 5. In both dendrites in Figure 1(B), dislocation channels are also visible where the shear bands initiated or terminated. Although slip in the crystalline phase is not visible in the APT data in Figure 5, close examination of the Be distribution shows Be segregation in a plane parallel to the shear direction in the dendrite, presumably decorating a dislocation channel.

The APT data show a denser and more complex distribution of shear bands that would not be visible from the TEM thin foils due to tilting requirements. In fact, the shear steps shown in Figure 5 are not parallel to each other but rather offset, which may be indicative of the slip system involved in deformation of the crystalline dendrite phase.

The observed deformed structures make the suggestion that in the BMGMCs studied, shear band formation is triggered by strong stress localization at the dendrite/glass interface, rather than from shear transformation zone-type matrix inhomogeneities. It is not the step at the interface that nucleates the shear band, but instead the formation of the shear band that produces the step through a coordinated process over a short time period, as further demonstrated elsewhere using detailed micromechanical modelling (Gibbons, 2016). Once a sufficient amount of free volume has accumulated along some path through the matrix, and the stress along this path is relatively high due to the irregular microstructure and accumulation of strain at the interface, the conditions are ripe for rapid shear localization in the form of a shear band. The shear band rapidly propagates across the amorphous matrix terminating at another dendrite. Further propagation of the shear band across multiple dendrites is blocked by the activation of multiple slip systems in the dendritic regions; blunting the intense shear localization. Furthermore, structural inhomogeneities and shear transformation zones in the glass, which in the absence of such externally (dendrite) driven stress localization control shear band formation, seem to play less of a role for strain localization in the amorphous phase of BMGMCs. Following the ductility of BMGMCs may be further improved by incorporating or engineering dendritic phases that can better dissipate large shear localizations through mechanisms such as micro-twinning or stress-driven martensitic transformations, as previously observed in select BMGC systems (Oh, 2011).

Conclusions

We illustrate a 3D characterization method for shear bands in metallic glasses based on APT. By accompanying STEM imaging and density-functional theory calculations, the apparent enhanced density, a technique artefact, is explained by an increase in the local work function that lowers the local evaporation field. This method allows full characterization

of the shear band structures, which we have examined for a $\text{Ti}_{48}\text{Zr}_{20}\text{V}_{12}\text{Cu}_5\text{Be}_{15}$ BMGMC.

Acknowledgements

The authors wish to acknowledge financial support from the Air Force Office of Scientific Research Award No. FA9550-12-1-0059 with partial support from Award No. FA9550-14-1-0249, from the University of Michigan College of Engineering, and from computational support by the Ohio Supercomputer Center under Grant No. PAS0072. Part of this research was carried out at the Jet Propulsion Laboratory, California Institute of Technology, under a contract with the National Aeronautics and Space Administration (NASA).

References

- Argon, A.S. (1979) Plastic deformation in metallic glasses. *Acta Metallurgica*. **27**(1), 47–58.
- Chen, G., Cheng, J.L. & Liu, C.T. (2012) Large-sized Zr-based bulk-metallic-glass composite with enhanced tensile properties. *Intermetallics* **28**, 25–33.
- Chen, J.H., Jiang, M.Q., Chen, Y. & Dai, L.H. (2013). Strain rate dependent shear banding behavior of a Zr-based bulk metallic glass composite. *Mat. Sci. Eng. A* **576**(0), 134–139.
- Chen, Y., Okhubo, T., Mukai, T. & Hono, K. (2009) Structure of shear bands in Pd40Ni40P20 bulk metallic glass. *J. Mat. Res.* **24**(1), 1–9.
- Donovan, P.E. & Stobbs, W.M. (1981) The structure of shear bands in metallic glasses. *Acta Metallurgica*. **29**(8), 1419–1436.
- Gibbons, M., Flores, K.M., Marquis, E.A., Windl, W. & Niezgoda, S.R. (2016) Shear banding in bulk metallic glass matrix composites with dendrite reinforcements. *Intl. J. Plasticity. In Review*.
- Guo, W., Jäggle, E.A., Choi, P.-P., Yao, J., Kostka, A., Schneider, J.M. & Raabe, D. (2014) Shear-induced mixing governs codeformation of crystalline-amorphous nanolaminates. *Phys. Rev. Lett.* **113**(3), 035501.
- Hays, C.C., Kim, C.P. & Johnson, W.L. (2000) Microstructure controlled shear band pattern formation and enhanced plasticity of bulk metallic glasses containing in situ formed ductile phase dendrite dispersions. *Phys. Rev. Lett.* **84**(13), 2901–2904.
- Jeon, C., Paul Kim, C., Seop Kim, H. & Lee, S. (2013) Dendrite size and tensile ductility in Ti-based amorphous alloys containing ductile dendrites. *Mat. Sci. Eng. A* **587**(0), 143–149.
- Jiang, W.H. & Atzmon, M. (2006) Mechanically-assisted nanocrystallization and defects in amorphous alloys: a high-resolution transmission electron microscopy study. *Scripta Materialia* **54**, 333–336.
- Kresse, G. & Hafner, J. (1994) Ab initio molecular-dynamics simulation of the liquid-metal amorphous-semiconductor transition in germanium. *Phys. Rev. B* **49**(20), 14251–14269.
- Laudon, M., Carlson, N.N., Masquelier, M.P., Daw, M.S. & Windl, W. (2001) Multiscale modeling of stress-mediated diffusion in silicon: Ab initio to continuum. *Appl. Phys. Lett.* **78**, 201–203.
- Li, J., Wang, Z.L. & Hufnagel, T.C. (2002) Characterization of nanometer-scale defects in metallic glasses by quantitative high resolution transmission electron microscopy. *Phys. Rev. B* **65**, 1442011–6.

- Lide, D.R. (2003) CRC Handbook of Chemistry and Physics, 84th edn. Section 10, Atomic, Molecular, and Optical Physics; Ionization Potentials of Atoms and Atomic Ions. CRC Press, Boca Raton, Florida.
- Miller, M.K. & Forbes, R.G. (2014) *Atom Probe Tomography: The Local Electrode Atom Probe*. Springer, New York.
- Müller, E. (1956) Field desorption. *Phys. Rev.* **102**(3), 618–624.
- Oh, Y.S., Kim, C.P., Lee, S. & Kim, N.J. (2011) Microstructure and tensile properties of high-strength high-ductility Ti-based amorphous matrix composites containing ductile dendrites. *Acta Materialia* **59**(19), 7277–7286.
- Perdew, J.P., Chevary, J.A., Vosko, S.H., Jackson, K.A., Pederson, M.R., Singh, D.J. & Fiolhais, C. (1992) Atoms, molecules, solids, and surfaces: applications of the generalized gradient approximation for exchange and correlation. *Phys. Rev. B* **46**(11), 6671–6687.
- Rösner, H., Peterlechner, M., Kübel, C., Schmidt, V. & Wilde, G. (2014) Density changes in shear bands of a metallic glass determined by correlative analytical transmission electron microscopy. *Ultramicroscopy* **142**, 1–9.
- Sanchez, C.G., Lozovoi, A.Y. & Alavi, A. (2004) Field-evaporation from first-principles. *Mol. Phys.* **102**(9–10), 1045–1055.
- Schneider, C.A., Rasband, W.S. & Eliceiri, K.W. (2012) NIH Image to ImageJ: 25 years of image analysis. *Nat. Meth.* **9**(7), 671–675.
- Shao, Y., Yao, K., Li, M. & Liu, X. (2013) Two-zone heterogeneous structure within shear bands of a bulk metallic glass. *Appl. Phys. Lett.* **103**, 171901–3.
- Smith, L. (1930) The emission of positive ions from tungsten and molybdenum. *Phys. Rev.* **35**(4), 381–395.
- Tsong, T.T. (1978) Field-ion image-formation. *Surf. Sci.* **70**(1), 211–233.
- Yao, L., Withrow, T., Restrepo, O.D., Windl, W. & Marquis, E.A. (2015) Effects of the local structure dependence of evaporation fields on field evaporation behavior. *Appl. Phys. Lett.* **107**, 241602–4.
- Zhang, T., Ye, H.Y., Shi, J.Y., Yang, H.J. & Qiao, J.W. (2014) Dendrite size dependence of tensile plasticity of in situ Ti-based metallic glass matrix composites. *J. Alloys Compounds* **583**(0), 593–597.
- Zhang, Y. & Greer, A.L. (2006) Thickness of shear bands in metallic glasses. *Appl. Phys. Lett.* **89**, 071907–9.